Chapter 4

Discussion

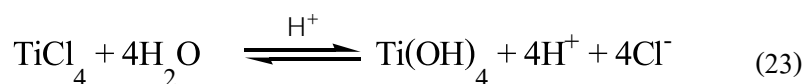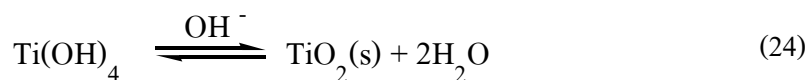### 4.1 Synthesis and characterization of titanium dioxide

4.1.1 Synthesis of undoped TiO_2 and trivalent (Al, B)-doped TiO_2

In general, the sol-gel process consists of the hydrolysis and condensation reactions which are catalysed in the presence of acid. The hydrolysis reaction leads to the formation of original nuclei of titanium dioxide while the condensation reaction leads to the growth of network system of original nuclei (Kumar et al., 1999). The general reactions are as follows.

The hydrolysis reaction

$$TiCl_4 + 4H_2O \xrightleftharpoons{H^+} Ti(OH)_4 + 4H^+ + 4Cl^- \qquad (23)$$

The condensation reaction

$$Ti(OH)_4 \xrightleftharpoons{OH^-} TiO_2(s) + 2H_2O \qquad (24)$$

Zhang et al., (2000) suggested the equilibrium between the hydrolysis reaction (nucleation stage) and the condensation reaction (growth stage) made the formation of titanium dioxide particles in the rutile phase possible. After the neutralization of ammonia solution, the equilibrium between the hydrolysis and condensation was broken and the condensation reaction or the growth rate was possible to accelerate the formation of anatase phase (Zhang et al., 2000). According to Tang et al., (2002), the formation of anatase and rutile titanium dioxide is determined by the hydrolysis and condensation reactions. If the condensation starts before completion of hydrolysis, either amorphous or anatase titanium dioxide will form. And also, in neutral and basic conditions, condensation starts before complete hydrolysis, while acid condition promotes the hydrolysis and decreases the condensation (Tang et al., 2002).

In the present work, it could be seen that rutile-only phase (undoped TiO_2 sample), anatase only phase and some Al peaks in XRD pattern (Al-doped TiO_2 samples), and mixture of anatase and rutile (B-doped TiO_2 samples) were obtained. It could be suggested that these products might have formed by the different reaction mechanism as described below.

For the case of undoped TiO_2, the reaction that carried out with the heating of titanium tetrachloride aqueous solution at 95^oC could be considered as a two-step processes, hydrolysis and condensation reactions. To promote the condensation step, the reaction was carried out at pH 7, by addition of NH_3 solution, because it was close to the point of zero-charge (PZC) of titanium dioxide at pH about 6.8. At this point, titanium dioxide has a neutral surface ($O^-OH_2^+$) with minimal electronic repulsion among particles; thus the rates of coagulation of titanium dioxide particles are the fastest and an equilibrium is also reached easily to give titanium dioxide crystalline (O'Sheam, et al., 1999). Moreover, the reaction appeared in the prolonged time (26 h.) because titanium dioxide crystalline could grow larger and more stable than shorter time (Yanqing et al., 2001). As seen in this study that only the rutile phase appears in undoped TiO_2 sample, this could be attributed to only the equilibrium between hydrolysis and condensation is appeared in this sample which result from the low volume of water in the reaction stabilized the equilibrium between hydrolysis and condensation reactions.

In Al-doped TiO_2 samples, the reaction consists of two-step processes, hydrolysis and condensation reactions. The activity of Al-doped TiO_2 is strongly influenced by the Al dopant content, and many other experimental parameters such as hydrolysis catalyst, amount of water and calcination. In this study, Al-doped TiO_2 samples were prepared with Al dopant content ranging from 0.04 to 0.32 mol% Al (which are designated as : 1_Al/ TiO_2 = 0.04 mol%, 2_Al/ TiO_2 = 0.08 mol%, 3_Al/ TiO_2 = 0.16 mol%, 4_Al/ TiO_2 = 0.32 mol%). Two samples consist of mixed anatase and rutile phases and two samples (3_Al/ TiO_2 and 4_Al/ TiO_2) consist of mixed anatase phase and the phase of aluminium oxonium sulfate hydrate $[(H_2O)Al_3(SO_4)_2(OH)_6]$. This could be explained that the equilibrium between hydrolysis and condensation reaction was broken by adding Al dopant which resulted in faster condensation and slower hydrolysis reaction. As a result, the possibility to form structure unit of anatase phase was obtained. In the studing of types of acid and amount of water in Al-doped TiO_2 samples, most samples showed anatase phase, but some samples consisted of mixed anatase and rutile phases. These could be explained that the equilibrium between hydrolysis and condensation reaction was also broken by the addition of these additives.

For the case of B-doped TiO_2 samples, the reaction could be considered as two-step processes, hydrolysis and condensation reactions. The effect of B_2O_3 on TiO_2 was strongly influenced by many experimental parameters such as hydrolysis catalyst, amount of water and calcination temperatures. All of these B-doped TiO_2 samples consisted of mixed anatase and rutile

phases. The results could be explained that the equilibrium between hydrolysis and condensation reaction was also broken which resulted in faster condensation and slower hydrolysis reaction.

4.2 Characterization of titanium dioxide

4.2.1 X-ray diffractometry (XRD)

The crystalline structures of the phases in these as-prepared sample were obtained by x-ray powder diffractometry which is shown in Figure 18 and Figure 19. From the XRD patterns, it could be seen that titanium dioxide in rutile or mixture of anatase and rutile phases was obtained as the reaction product at low temperature about $95^{\circ}C$. In the case of undoped TiO_2 sample showed only pure rutile phase. For Al-doped TiO_2 samples (Figure 18), some were mixture of anatase and rutile phases, some were only anatase phase, and some were Al phase in the XRD pattern. In the case of B-doped TiO_2 samples (Figure 19), most of these samples showed mixed anatase and rutile phases. From the XRD measurement, the information on the size of anatase and rutile crystallites were also obtained by using the Scherrer formula which is generally the accepted method to estimate the average crystallite size (Ohtani et al., 1997). The data of crystallite size of the anatase and rutile phase of Al-doped TiO_2 samples and B-doped TiO_2 samples are shown in Table 8 and Table 9, respectively. These results demonstrated that the crystallite size is found to be in nanometer region. It should be noticed that the XRD spectra of these synthesized TiO_2 samples are broad and weak indicating the predominantly amorphous phase being present in the these synthesized samples. The broad and weak peaks in XRD spectrum of these synthesized TiO_2 samples indicated that these samples were nanoparticles (Liqiang et al., 2003).

The XRD patterns of Al-doped TiO_2 and B-doped TiO_2 samples calcined at different temperature for 3 h are shown in Figure 18(d) and Figure 19(d), respectively. The phases of these as-prepared TiO_2 samples calcined at 400, 500, 600, 700, $800^{\circ}C$ are the mixture of anatase and rutile phases. In addition the grain sizes get larger with the increasing calcination temperature (Cun et al., 2002). These results agreed with the data in Table 8 and Table 9. Calcination is a common treatment that can be used to improve the crystallinity of TiO_2 powders. The data from Table 10 and Table 11 show that the percentage of anatase and rutile phases of trivalent (Al, B)-doped TiO_2 samples increase with the increasing calcination temperature. It may be noticed that rutile phase began to form at low temperature and was the dominant phase with increase in the calcination temperature. In fact the anatase to rutile transformation has been extensively reported in

the literature and the anatase to rutile transformation in TiO_2 is known to be affected by crystalline size, dopant type and concentration, as well as the titanium precursor used in solution chemical synthesis. The phase transformation of anatase to rutile is nucleation at anatase twin boundaries. Rutile nucleation involves displacement of only half the titanium cations in the twin slab. As the transformation continues, slabs of anatase octahedral are destabilized. The destabilization will result in a rapid progression of anatase into rutile. It is known that the surface energy of rutile is significantly larger than that of anatase and any increase in nucleation sites will favor the anatase to rutile transformation. Based on our XRD results, it may be seen that the average crystallite size of TiO_2 nanoparticles has a great influence on anatase to rutile transformation. This means that when the anatase has a very fine crystallite size, more nucleation sites will form and anatase to rutile transformation tendency increases. In present work, the rutile phase occures at relatively low temperature in both cases of Al-doped TiO_2 and B-doped TiO_2 samples. The resulting in present work has corresponsed to those observed by Yang and Ferreira (1998). They also studied the inhibitory effect of the mixed alumina and silica additives with molar ratios of [Al]/[Ti] = 0.05 and [Si]/[Ti] = 0.05 on the phase transformation of anatase to rutile. The suppressing effect on the anatase-rutile transformation by mixed additives was observed to be much stronger than that of the single additive. The formation of the anatase solid solution with both alumina and silica was probably responsible for the stronger inhibitory effect. The retarding effect on the anatase-rutile transformation is shown in Figure 53 (Yang et al., 1998). Therefore these results indicated that these trivalent (Al, B)-doped TiO_2 samples could be influenced in the retarding effect on the anatase to rutile phase transformation.
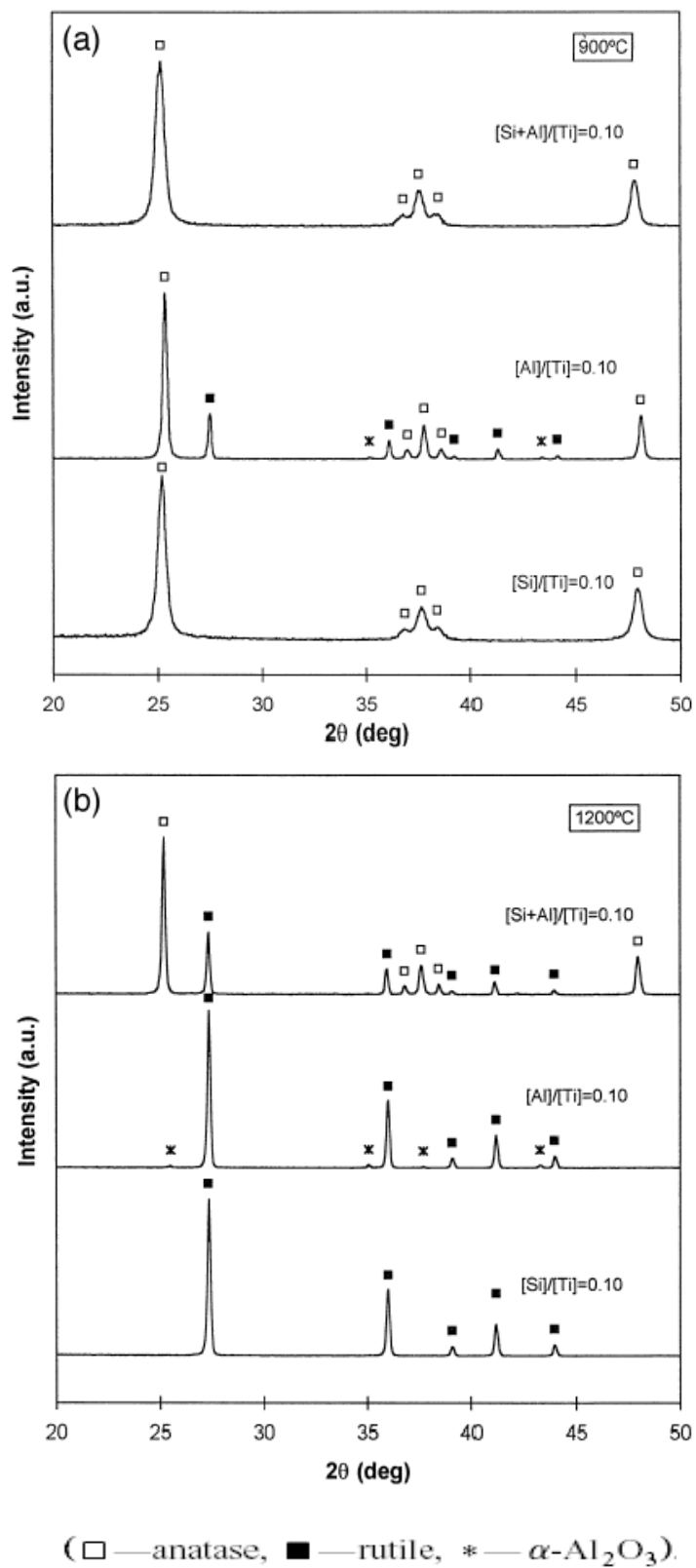
Figure 53 XRD patterns of the titania powders with various additives after being calcined at

a) 900°C and b) 1200°C for 1 h. (Yang et al., 1998 : 322)

The effect of amount of dopants in Al doped TiO_2 samples show that Al dopants are found in XRD pattern (Figure 18(a)) in 3_Al/TiO_2 and 4_Al/TiO_2 sample in the form of aluminium oxonium sulfate hydrate [(H_2O)Al_3(SO_4)$_2$(OH)$_6$]. This results indicated that Al^{3+} could enter into TiO_2 lattice to substitute for Ti^{4+}. This was possible because the radius of Al^{3+} (0.68 Å) was only slightly larger than that of Ti^{3+} (0.64 Å).

The differences in the crystallographic phase of these trivalent (Al, B)-doped TiO_2 samples can be attributed to different in ratio of volume of water to titanium tetrachloride (H_2O/$TiCl_4$) under the same conditions. It can be seen that only rutile phase was obtained at [H_2O/$TiCl_4$] = 2.5 (Figure 19b : 50w_B/TiO_2), whereas a mixture of anatase and rutile was obtained when the volume ratio were 5, 7.5, and 10 (Figure 19b : 100w_B/TiO_2, 150w_B/TiO_2, 200w_B/TiO_2, respectively), as found in B-doped TiO_2 samples . These results indicated that the amount of water determined the structure of the samples. For Al-doped TiO_2 samples, a mixture of anatase and rutile was obtained at [H_2O/$TiCl_4$] = 2.5 (Figure 18b : 50w_Al/TiO_2), whereas only anatase phase was obtained when the volume ratio were 5, 7.5, and 10 (Figure 18b : 100w_Al/TiO_2, 150w_Al/TiO_2, 200w_Al/TiO_2, respectively). These results from these trivalent (Al, B)-doped TiO_2 samples corresponded to those observed by Ding et al., (1997) who studied the hydrolysis reaction of Ti(O-Bu)$_4$ with water. They found that the amount of water determined the chemical and structure changes of the gel-derived titanium dioxide powders (Ding et al.,1997). But their results were different from this study in term of structure stability that the sample prepared by smaller amount of water has more stable phase of anatase than those with larger amount of water. They only discussed that the difference in amount of water determined the degree of hydrolysis which directly responsible for the structure of TiO_2. Their result was opposite to this study where it was found that rutile is more stable than mixed anatase and rutile phases at lower amount of water of B-doped TiO_2 samples, and the mixed anatase and rutile phases of Al-doped TiO_2 samples is more stable than the anatase phase, as evidenced from XRD study. The different of phase stability may be the result of starting material, metal dopant and also from the volume of water for the preparation of titanium dioxide which may affect the crystal structure of sample.

Yanagisawa and Overtone et al., (1999) also studied the effect of water for the crystallization of anatase by using dry vapor and hydrothermal conditions. Their results showed that in all cases where water was present (200 mL, 300 mL), anatase was produced, with no rutile

present. They discussed that the presence of water in the reaction catalyzed the crystallization step of anatase structure (Yanagisawa and Overtone., 1999). However, they did not demonstrate the effect of water content on the crystallization of titanium dioxide. Their results did not agree with this work which found the present of rutile phase in these trivalent (Al, B)-doped TiO_2 samples as evidenced by XRD pattern showed in Figure 18b and Figure 19b. The change in the crystalline structure of titanium dioxide could be due to the different in preparation method. Thus, the change in the amount of water could affect the crystallinity of titanium dioxide and sometime it may be also responsible for the porous properties (Samantaray et al., 2003).

The effect of synthesis additives (HCl, CH_3COOH, HNO_3, H_2SO_4, H_3PO_4) during the sol-gel process of these trivalent (Al, B)-doped TiO_2 samples, showed the phase of sample measured by XRD technique, see Figgure 18c and Figure 19c, and summarized in Table 24. These results showed that the type of catalysts added during hydrolysis reaction influences the phase structures and crystallization of these synthesized TiO_2 powders at $95^{\circ}C$. In addition, the adding of H_3PO_4 additive enhances the crystallization of anatase in both trivalent (Al, B)-doped samples ($H_3PO_4\_Al/TiO_2$ and $H_3PO_4\_B/TiO_2$). Some results are different from that observed by Terabe et al., (1994) who found only anatase phase in the powders prepared with HCl catalyst. They claimed that the anatase phase is more stable than the amorphous phase in acidic solutions (Terabe et al.,1994).

So et al.,(1998) studied the crystalline phase of titania, they prepared using a sol-gel method followed by a peptizing treatment with HNO_3. They found that both anatase and rutile could be formed even at room temperature (So et al.,1998). Escobar et al., (2000) investigated Al_2O_3-TiO_2 materials prepared by sol-gel method using different additives (HNO_3, NH_4OH, and CH_3COOH). They found that the complexing (CH_3COOH) and the basic (NH_4OH) additives led to solid with high surface area and pore volume. HNO_3 catalyzed samples showed lower surface areas and pore volumes. The XRD results showed all the dried and calcined materials (up to a temperature of 973 K) were amorphous (Escobar et al., 2000).

Table 24 Phase of these trivalent (Al, B)-doped TiO_2 samples by adding synthesis additives.

TiO_2 samples	Phase of sample
Al-doped TiO_2 samples	
CH_3COOH_Al/ TiO_2	anatase
HCl_Al/ TiO_2	anatase
HNO_3_Al/ TiO_2	anatase + rutile
$H_2SO_4\_Al/ TiO_2$	anatase + rutile
$H_3PO_4\_Al/ TiO_2$	anatase
B-doped TiO_2 samples	
CH_3COOH_B/ TiO_2	anatase + rutile
HCl_B/ TiO_2	anatase + rutile
HNO_3_B/ TiO_2	anatase + rutile
$H_2SO_4\_B/ TiO_2$	anatase + rutile
$H_3PO_4\_B/ TiO_2$	anatase

4.2.2 Surface area and pore size

The specific surface areas of Al-doped TiO_2 samples and B-doped TiO_2 samples were shown in Table 12 and Table 13, respectively. In order to compare this value, the undoped TiO_2 and these trivalent (Al, B)-doped TiO_2 samples were also subjected to the same measurement under the same conditions. It can be seen in Table 12 that most of these Al-doped TiO_2 samples (amount_Al/TiO_2, water_Al/TiO_2, acid_Al/TiO_2) have higher surface area than the undoped TiO_2 due to lower crystallinity of the synthesized samples. The data of calcined_Al/TiO_2 showed that the increased calcination temperature, resulted in the decreased in surface area, due to increasing in crystallinity. Most of B-doped TiO_2 samples (amount_B/TiO_2, water_B/TiO_2, acid_B/TiO_2) have higher surface area than the undoped TiO_2, except 50w_B/TiO_2 sample, it showed slightly smaller surface area (109.36 m^2/g) than the undoped TiO_2 (115.90 m^2/g). Furthermore, these data of calcined_B/TiO_2 also showed that the increased calcination temperature, decreased in surface area. These results of these trivalent (Al, B)-doped TiO_2 samples are in agreement with SEM study which shows the morphology of these synthesized TiO_2 samples. The smaller particle sizes and highly

aggregration of sample could be attributed to higher surface area. Calcination of the samples have increased the sized of the particles and also decreased their specific surface areas.

The porous nature of synthesized titanium dioxide was studied by nitrogen adsorption isotherm. In order to ultilize the information within the adsorption isotherms, it is necessary to consider the shape of physisorption isotherm and the identification of the principle mechanism of adsorption. The majority of physisorption isotherms could be grouped into six types, as shown in Figure 54. The IUPAC classification of the pore are shown in Table 25.

The Type I isotherm is given by microporous solids. The very steep region at low P/P_o is due to the filling of very narrow pores and limiting uptake is dependent on the accessible micropore volume rather than on the internal surface area. The Type II isotherm is normally given by a non-porous solids which unrestricted monolayer-multilayer adsorption can occur. The Type III isotherm is generally associated with weak adsorbent-adsorbate and relatively strong adsorbate-adsorbate interactions. In this case cooperative effects lead to the development of patches of multilayer before a uniform monolayer has been formed. Type IV isotherm with hysteresis loop is the characteristic features of the adsorbate-absorbate interactions which is associated with capillary condensation. Some microporous or mesoporous solids are amongst the few adsorbents to give Type V isotherm. The Type VI isotherm is relatively rare, it presents stepwise multilayer adsorption on a uniform non-porous surface (Ryu et al., 1999).
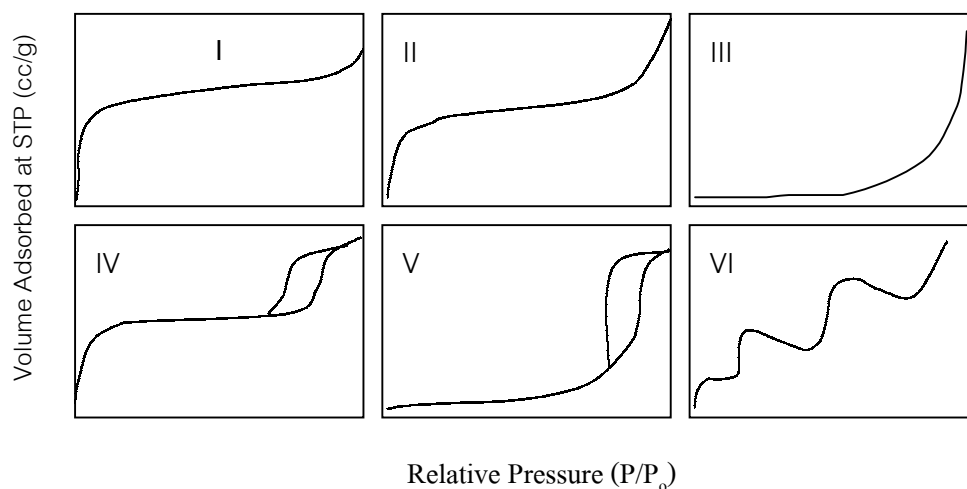

Figure 54 IUPAC classification of adsorption isotherms (Ryu et al., 1999).

Table 25 IUPAC classification of the pore (Khalil et al., 2001).

Porosity type	Size(d)
Ultramicropores	< typical molecule diameter of the adsorptive about 0.6 nm
Micropores	d < 2 nm
Mesopores	2 nm < d < 50 nm
Macropores	d > 50 nm

The nitrogen adsorption isotherms for Al-doped TiO_2 samples and B-doped TiO_2 samples are shown in Figures 20 and 21, respectively. The isotherms corresponding to these Al-doped TiO_2 samples and B-doped TiO_2 samples are a combination of Type I and IV (BDDT classification) (Ryu et al., 1999) with two distinct regions; at low relative pressure, the isotherm exhibits high adsorption, indicating that the sample contains micropore (Type I). However, at high relative presure, the curve exhibits the presence of mesopores (Type IV). In this study, the hysteresis loop in the isotherm could not be determined due to the limited capability of the equipment (SA3100 coulter) which was not able to determine the desorption study. The present of micropore could be checked by plotting the adsorbed layer called "*t*-plot" as seen in Figures 22 and 23 for Al-doped TiO_2 samples and B-doped TiO_2 samples, respectively. It seems that for some of these synthesized TiO_2 samples, there is an early linear section passing the origin. This behavior indicated that the specimen lacks of micropore but contains only mesopores (Khalil et al., 2001). However, *t*-plot of most samples show that linear section is not pass the origin, suggesting that it contains not only mesopore but also micropore (Khalil et al., 2001).

The isotherm type and porosity type of these Al-doped TiO_2 samples and B-doped TiO_2 samples are shown in Table 26 and Table 27, respectively. The pore size distribution of synthesized Al-doped TiO_2 samples and B-doped TiO_2 are shown in Figures 24 and 25, respectively. The Al-doped TiO_2 samples show bimodal pore size distribution consisting of intra-particle pores (4-8 nm) and larger inter-particle pores (8-100 nm). Usually, there are two types of pores present in the bimodal pore size distribution. One is made from the intra-aggregated pores at lower P/P_o range (the pores within the hard aggregates) and the other is larger inter-aggregated pores in the higher

P/P_o range arising from hard aggregated (the void between hard aggregates) (Yu et al., 2003). For B-doped TiO_2 samples, most of samples exhibit bimodal pore size distribution, but the other samples (calcined_ B/TiO_2, 50w_ B/TiO_2) show monomodal pore size distribution due to the collapse of the intra-particle pores. In the case of undoped TiO_2 sample, it found monomodal pore size distribution. The main cause of the disappearance of intra-particle pores could be attributed to the non-growth of anatase, leading to the disappearance of the void among anatase crystallite which results in the collapse of intra-particle pores.

As seen in the study of Yu et al., (2003) who investigated the microstructures of titanium dioxide powders doped F^- at various temperatures by scanning electron microscope. They found that after calcined at 700^oC, the intra-particle pores of pure and doped titanium dioxide completely disappeared. This could be attributed to grain growth from the phase transformation of anatase to rutile, leading to the disappearance of the intra-particle pores. Furthermore, they also studied the pore size distributions of Degussa P25 titania powders prepared by flame hydrolysis of $TiCl_4$. The P25 powder has small specific surface area ($53.2 \text{ m}^2/\text{g}$). It also shows a totally different pore-size distribution. The pore structure of the P25 powder is monomodal of larger inter-particle pores (8-100 nm) with a maximum pore diameter at 34 nm (Yu et al., 2003).

Table 26 The isotherm type and porosity type of Al-doped TiO_2 samples

TiO_2 samples	Isotherm type	Porosity type
undoped TiO_2	Type I and IV	micropore+mesopore
a)amount_Al/TiO_2		
1_Al/TiO_2	Type I and IV	micropore+mesopore
2_Al/TiO_2	Type I and IV	micropore+mesopore
3_Al/TiO_2	Type I and IV	micropore+mesopore
4_Al/TiO_2	Type I and IV	micropore+mesopore
b)water_Al/TiO_2		
50w_Al/TiO_2	Type I and IV	micropore+mesopore
100w_Al/TiO_2	Type I and IV	micropore+mesopore
150w_Al/TiO_2	Type IV	mesopore
200w_Al/TiO_2	Type IV	mesopore
c)acid_Al/TiO_2		
CH_3COOH_Al/TiO_2	Type I and IV	micropore+mesopore
HCl_Al/TiO_2	Type I and IV	micropore+mesopore
HNO_3_Al/TiO_2	Type I and IV	micropore+mesopore
H_2SO_4_Al/TiO_2	Type I and IV	micropore+mesopore
H_3PO_4_Al/TiO_2	Type IV	mesopore
d)calcined_Al/TiO_2		
400c_Al/TiO_2	Type IV	mesopore
500c_Al/TiO_2	Type IV	mesopore
600c_Al/TiO_2	Type IV	mesopore
700c_Al/TiO_2	Type IV	mesopore
800c_Al/TiO_2	Type IV	mesopore

Table 27 The isotherm type and porosity type of B-doped TiO_2 samples

TiO_2 samples	Isotherm type	Porosity type
undoped TiO_2	Type I and IV	micropore+mesopore
a)amount_B/TiO_2		
0.5wt_B/TiO_2	Type IV	mesopore
1.0wt_B/TiO_2	Type IV	mesopore
2.0wt_B/TiO_2	Type IV	mesopore
3.0wt_B/TiO_2	Type IV	mesopore
4.0wt_B/TiO_2	Type IV	mesopore
5.0wt_B/TiO_2	Type IV	mesopore
10.0wt_B/TiO_2	Type IV	mesopore
b)water_B/TiO_2		
50w_B/TiO_2	Type I and IV	micropore+mesopore
100w_B/TiO_2	Type I and IV	micropore+mesopore
150w_B/TiO_2	Type I and IV	micropore+mesopore
200w_B/TiO_2	Type IV	mesopore
c)acid_B/TiO_2		
CH_3COOH_B/TiO_2	Type IV	mesopore
HCl_B/TiO_2	Type IV	mesopore
HNO_3_B/TiO_2	Type IV	mesopore
H_2SO_4_B/TiO_2	Type I and IV	micropore+mesopore
H_3PO_4_B/TiO_2	Type IV	mesopore
d)calcined_B/TiO_2		
400c_B/TiO_2	Type IV	mesopore
500c_B/TiO_2	Type IV	mesopore
600c_B/TiO_2	Type IV	mesopore
700c_B/TiO_2	Type IV	mesopore
800c_B/TiO_2	Type IV	mesopore

4.2.3 Fourier-transformed infrared spectrophotometry (FT-IR)

The infrared spectra of these synthesized trivalent (Al, B)-doped TiO_2 samples in the range 4,000-400 cm^{-1} are shown in Figures 26 and 27. The band at around 3,180 cm^{-1} which shown in these figures is the stretching vibration of O-H bonding (in Ti-OH) which could not be removed easily until at relatively higher temperature (Wang et al., 2000). Near this band at 3,050 cm^{-1}, a shoulder was generated by an asymmetric vibration mode of the residual ammonium ions (Sanobez et al., 1996). The intensity of the 3,180 cm^{-1} band was high, suggesting that the O-H bonding (in Ti-OH) dominated the sol-gel reaction (Sanobez et al., 1996). This result supports the fact that the current reaction favors hydrolysis and slow condensation since titanium dioxide crystallines were very small, the local environment of the O-H bonding (in Ti-OH) was not homogeneous, widening the 3,180 cm^{-1} band. The bending vibration of the O-H bonding (in Ti-OH) appeared at around 1,642 cm^{-1} for these synthesized samples (Velasco et al., 1999).This band corresponds to adsorbed molecular water (Navio et al., 1996) which associated with deformation vibration for H-O-H bonds of the physisorbed water (Li et al., 2005). The structures proposed for the physisorbed water on TiO_2 surface are shown in Figure 55.
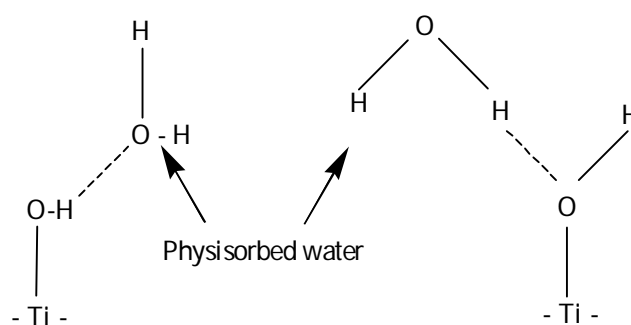

Figure 55 The proposed structures for the physisorbed water on TiO_2 surface (Li et al., 2005).

The IR band in the range of 1280–1650 cm^{-1} are vibrational lines of the HCO_3^- and CO_3^{2-} group that are shown in Figure 26m and Figure 27m (Harizanov et al., 2001). FT-IR spectra of sulphate metal oxides generally show a strong absorption band at 1381 cm^{-1}, and broad bands at 1250-1100 cm^{-1} (Figure 26k and Figure 27k). The band at 1381 cm^{-1} is the streching frequency of S-O, and the 1250-1100 cm^{-1} bands are the characteristic frequencies of SO_4^{2-}. When SO_4^{2-} is bound to the titania surface, the symmetry can be split into three bands (1221, 1119, and 1026 cm^{-1}) was assigned to the bidentately bound sulphate group (Samantary, et al., 2003). In the low energy region (900-400

cm^{-1}), the band due to stretching mode of Ti-O could be assigned. The presence of band in this spectral region could be assigned the crystalline structure (anatase or rutile phase) of titanium dioxide (Valesco et al., 1999). These synthesized samples shows the band at 470 cm^{-1} corresponding to Ti-O stretching mode of rutile structure (Zhang et al., 2001). The character of bands at 414 cm^{-1} indicated that sample consists of the mixture phases of anatase and rutile (Zhang et al., 2001). In addition, some of these synthesized TiO_2 samples also had bands at 665 and 468 cm^{-1} due to the crystalline phases of anatase and rutile, respectively. Thus, the IR studies indicated that only rutile or mixture of anatase and rutile phases resulted under sol-gel conditions. From an assignment of the FT-IR bands, it suggested that the undoped TiO_2 sample should exist in the mixed form of TiO_2 (rutile) and $[Ti(H_2O)_x(OH)_2]^{2+}$ (amorphous), and these synthesized trivalent (Al, B)-doped TiO_2 samples in TiO_2 (anatase and rutile) and $[Ti(H_2O)_x(OH)_2]^{2+}$ (amorphous) (Shao et al., 2001). This summary helps explain that these synthesized samples have low crystallinity with high content of amorphous.

4.2.4 Thermogravimetric analysis (TGA)

The results of TGA analysis of these synthesized samples also indicated that the difference in the adding amount of dopant, volume of water, type of acid, and calcined temperature influences the decomposition behavior. The undoped TiO_2 sample shows the decomposition of adsorbed water at the temperature below 700°C. The loss of weight was not very obvious at the temperature after 700 $^{\circ}$C which possibly resulted from the desorption of the hydroxyl group (of Ti-OH) on the particle (Liqiang et al., 2003). The greater weight loss found in these synthesized trivalent (Al, B)-doped TiO_2 samples indicated that there was larger amount of hydroxyls as free water and impurity in sample (Ding et al., 1997). It is known that there are two types of surface hydroxyl groups, i.e. terminal Ti-OH and bridge Ti(OH)Ti. Dissociation temperature of these surface hydroxyl groups differs from each other and each temperature also could be affected by the chemical surrounding. Thus, the decrease in the weight appears at the wide range of temperature (Yoshio et al., 1998). For these synthesized trivalent (Al, B)-doped TiO_2 samples, the weight loss registered below 250°C could be attributed to the removal of both physisorbed water and the solvent (Escobar et al., 2000). The weight loss of these synthesized TiO_2 samples in second stage from 250 to 400 $^{\circ}$C corresponds to the oxidation of residual organic components and removal of

chemically adsorbed water (Chang Song et al., 2000). It could be obvious in the 800c_B/TiO$_2$ sample, demonstrated that it is stable substance due to it could not decompose.

4.2.5 Differential thermal analysis (DTA)

According to differential thermal analysis curves of these as-prepared samples, it could be found that the endothermic peak around 100°C assigned to the expulsion of free adsorbed water from sample which is more prominent in these synthesized samples (Liqang et al., 2003). This is in confirmation with the TGA analysis which shows weight loss in these as-prepared samples. An endothermic peak at around 250°C associated with the removal of water and combustion decomposition of the organic matters (Liqang et al., 2003). The exothermic peak at around 400 $^{\circ}$C (Al-doped TiO$_2$ samples), 450 $^{\circ}$C (B-doped TiO$_2$ samples), 550 $^{\circ}$C (undoped TiO$_2$ sample) indicated the phase transformation of TiO$_2$ gel from amorphous to anatase. The phase transformation from anatase to rutile appears around 800°C (undoped TiO$_2$, and B-doped TiO$_2$ samples),and the exothermic peak in the range 850-1110 $^{\circ}$C for Al-doped TiO$_2$ samples. A resulting from the formation of corundum peak for all Al-doped TiO$_2$ samples. The area of peak could also suggest the content of amorphous in these synthesized samples. It could be seen that the exothermic peak of Al-doped TiO$_2$ samples and some of B-doped TiO$_2$ samples show the area of peak larger than the undoped TiO$_2$ sample. This mean that these synthesized trivalent (Al, B)-doped TiO$_2$ samples containing more amorphous than the undoped TiO$_2$ sample (Xie et al., 2002). Moreover, these trivalent (Al, B)-doped TiO$_2$ samples show broader exothermic peak of amorphous to anatase phase than that of the undoped TiO$_2$ sample which indicates that amorphous to anatase phase transformation of these synthesized trivalent (Al, B)-doped TiO$_2$ samples are slower than that the undoped TiO$_2$ sample (Xie et al., 2002).

4.2.6 Scanning electron microscope (SEM)

The SEM study gives only the information about the morphology and aggregation of particles. From SEM images of this study, which are shown in Figure 32 and Figure 33 for the data of Al-doped TiO$_2$ samples and B-doped TiO$_2$ samples, respectively. These result show the important difference in morphology of these trivalent (Al, B)-doped TiO$_2$ samples and the undoped TiO$_2$ sample. The undoped TiO$_2$ sample appears lower aggregation of spherical shape particle than these trivalent (Al, B)-doped TiO$_2$ samples and also have uniform structure. But for Al-doped TiO$_2$

samples, they appear a dense and smaller particle with highly aggregate than the undoped TiO_2 sample. In the case of amount_Al/TiO_2 samples, indicated that the Al dopants are highly coated on the surface of TiO_2 particles. It could be obvious in 3_Al/TiO_2 and 4_Al/ TiO_2 (Figure 32a(4b) and 32a(5b), showed the Al_2O_3 particles in these as-prepared samples. This result agrees with the XRD data. For water_Al/TiO_2 samples found that the volume of water may affect the aggregation of particle. This results show that larger amount of water (150w_Al/TiO_2 and 200w_Al/TiO_2) have lower aggregate than that the fewer volume of water (50w_Al/TiO_2 and 100w_Al/TiO_2). Furthermore, it could be obvious that the larger volume of water_Al/TiO_2 samples have bigger particle size than the fewer volume of water_Al/TiO_2 samples. In the case of acid_Al/TiO_2 samples, it shows that H_3PO_4_Al/TiO_2 sample appears dense and smaller uniform spherical particles than that the others acid_Al/TiO_2 samples. The effect of increasing calcination temperature, this results indicate more aggregate between group of particles than non-calcined sample, which are shown in Figures 32a(2a), 32d(1a), and 32d(2a). The morphology of some A-doped TiO_2 samples are similarly appeared to the results of Zhang et al., (2003) and Lee et al., (2004) shown in Figure 56 and compared with some of these Al-doped TiO_2 samples.

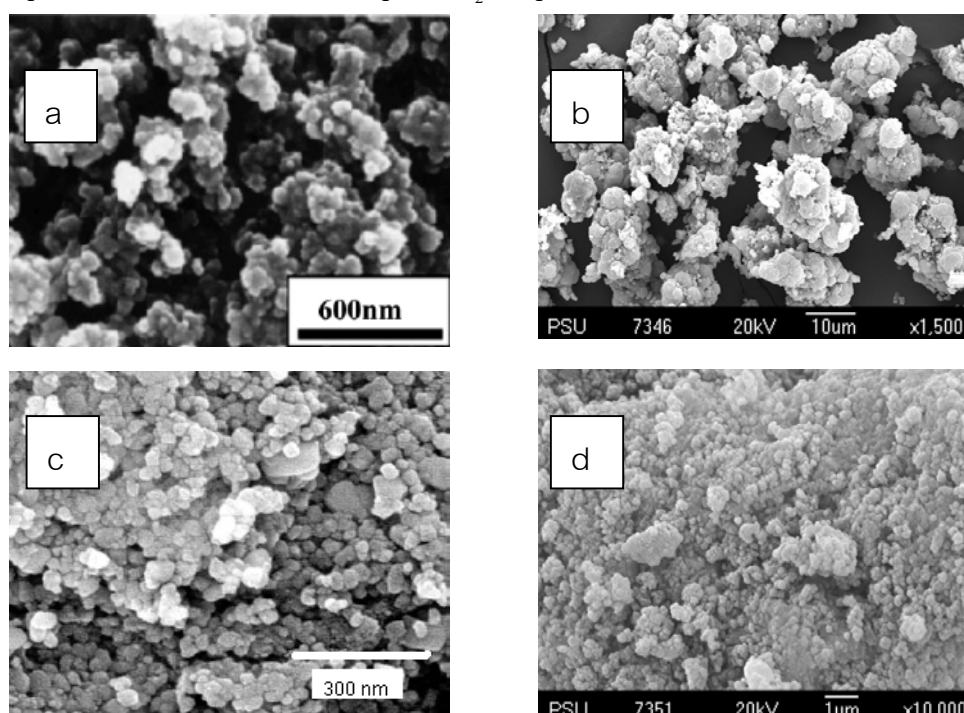**Figure 56** The SEM images of Al_2O_3/ TiO_2 samples : a) Al_2O_3/ TiO_2 sample from Lee et al.,

(2004), b) H_2SO_4_Al/ TiO_2 sample (this work), c) Al_2O_3/ TiO_2 sample from Zhang

et al.,(2003), and d) H_3PO_4_Al/ TiO_2 sample(this work).

In the case of amount_B/TiO$_2$ samples, at the lower B$_2$O$_3$ addition (0.5wt_B/TiO$_2$, 1.0wt_B/TiO$_2$), these samples have dense and highly aggregate of small spherical particle than that of higher amount of B$_2$O$_3$ (5.0wt_B$_2$O$_3$ and 10.0wt_B$_2$O$_3$) on TiO$_2$ surface, which are shown in Figures 33a(2a), 33a(3a), 33a(4a), and 33a(5a). For water_B/TiO$_2$ samples, it indicated that at larger amount of water the sample appears highly dense and non-uniform structure, shown in Figures 33b (1a) to 33b(4a). In the case of acid_B/TiO$_2$ and calcined_B/TiO$_2$ samples, they appear a dense and non-uniform structure (Figures 33c(1a) to 33c(5a)). For calcined_B/TiO$_2$ samples, indicated that high calcination temperature make larger dense sample than non-calcined sample, shown in Figures 33a(2a), 33d(1a), and 33d(2a).

The difference in the morphology could be ascribed to different preparation conditions, especially, the volume of water, the amount of dopants, the type of acids, and calcination temperature, these factors may affect the aggregation of each synthesized sample. The morphology of the dense synthesized sample is similar to the results of Yu et al., (2003) who investigated the effect of acidic and basic hydrolysis catalysts on the photocatalytic activity and microstructure of titanium dioxide prepared by sol-gel process. Their results showed that the morphology of titanium dioxide prepared by the hydrolysis of titanium tetraisopropoxide at pH 6.8 and without using HNO$_3$ as catalyst appears a dense structure and fewer in aggregation (Yu et al., 2003).
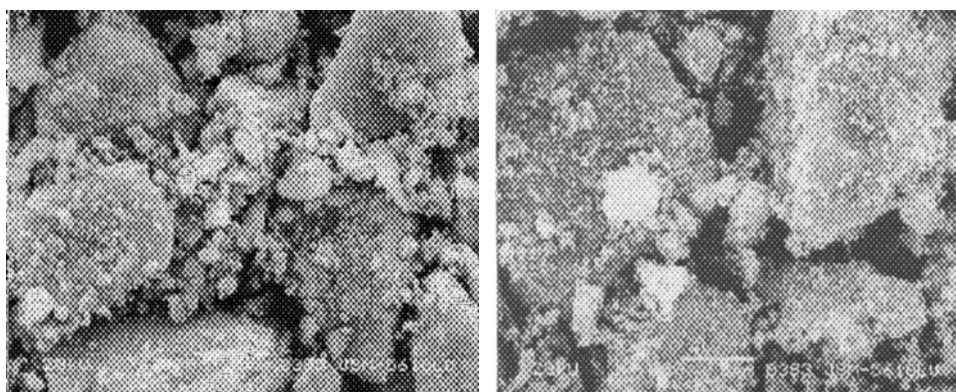

Figure 57 SEM images of TiO$_2$ from the study of Yu et al., (2003)

4.2.7   Transmission electron microscope (TEM)

The exact microstructure of the synthesized titanium dioxide could be investigated by TEM. The typical microstructure of the undoped TiO_2 sample (Figure 34a and 34b) showed that it only consisted of tenuous fibers of rutile which agreed with the study of Wang et al., (2001) who synthesized nanocrystalline rutile titanium dioxide in mixed organic solvents (alcohol and acetic acid) by hydrothermal method. They found that the product consisted of tenuous fibers of rutile as shown in Figure 58.
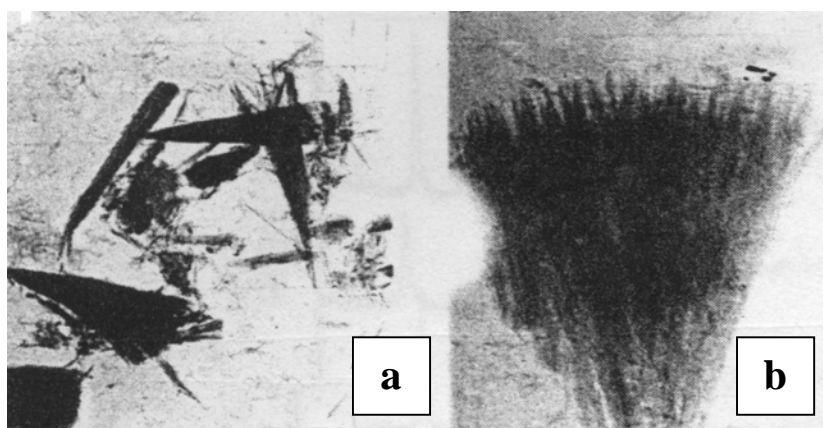

Figure 58 TEM images of rutile TiO_2; Wang et al., 2001 (a) tenuous fiber of rutile phase

(b) : higher magnification of the dark area in (a).

Other researchers suggested that rutile consisted of rod-like shape (Yang et al., 2002). The difference in microstructure of rutile could be due to the difference of preparation methods (Yang et al., 2002). For Al-doped TiO_2 samples, they show highly aggregate of ball-like particles and also have small amount of tenuous fibers of rutile (shown in Figures 34c and 34d). In the case of B-doped TiO_2 samples, they have two shapes owing to the formation of the mixed phase of anatase and rutile phase. The results of TEM images showed that B-doped TiO_2 sample consisted of ball-like of anatase and also rod-like structure of rutile (Yang et al., 2002). The TEM photos of TiO_2 powder prepared by Yang et al.(2002) showed in Figure 59. Furthermore, this results correspond to the study of Seo et al., (2001) who prepared titanium dioxide in anatase and rutile phases from the reaction of $TiOCl_2$ and NH_4OH and then aging in 0.5 M HCl for 24 h. Their study showed that the product consisted of anatase and rutile phases with spherical and tenuous fibers shaped of anatase and rutile, respectively.
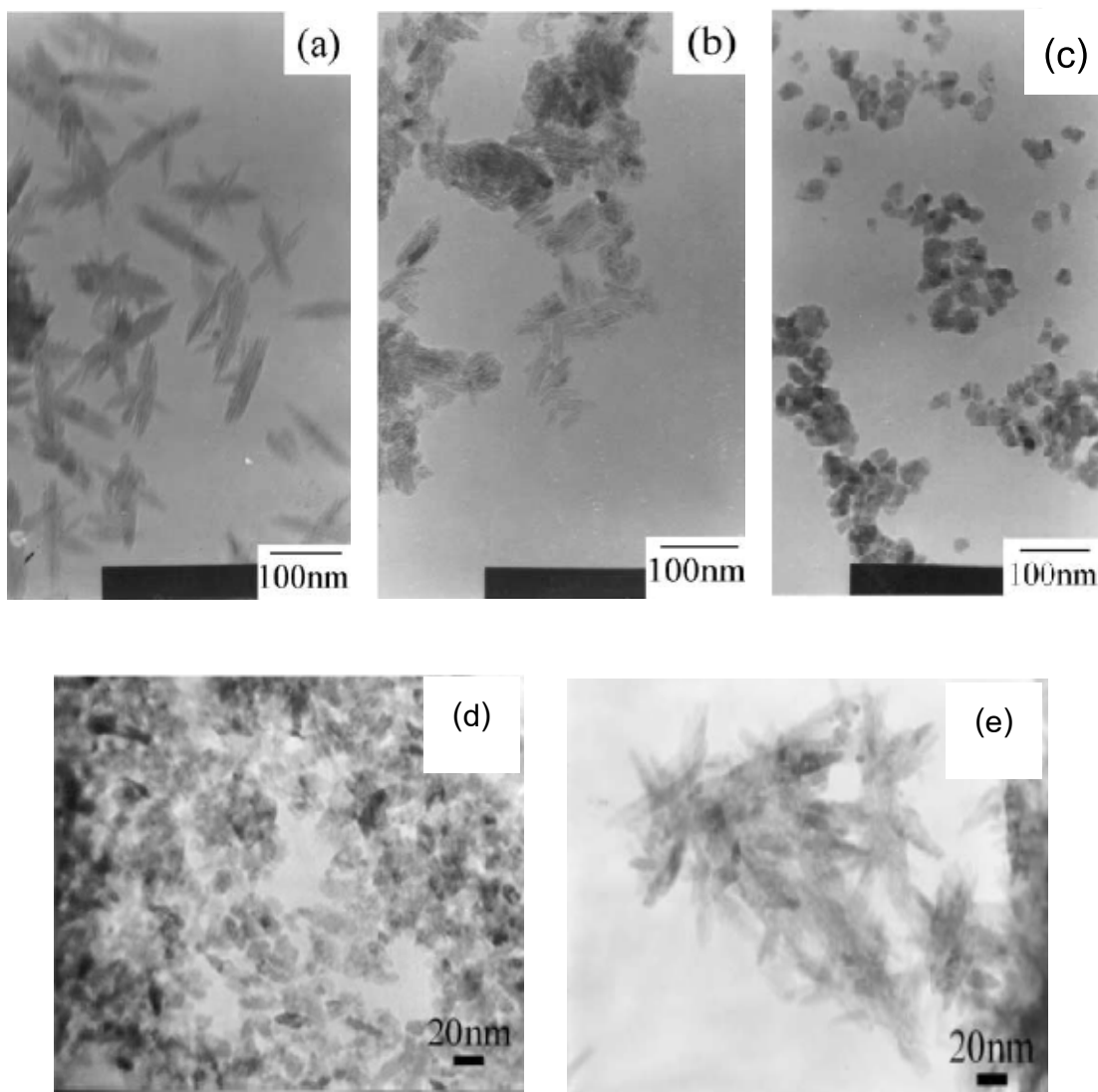
Figure 59 TEM photos of TiO_2 ; a-c (Yang et al., 2002) and d-e (Seo et al., 2001).

4.2.8 Ultraviolet-visible spectroscopy (UV-VIS)

UV-Vis spectroscopy has been used to characterize the bulk structure of crystalline titanium dioxide. Titanium dioxide is a semiconducting oxide with easily measured optical band gap. UV-Vis diffused reflectance spectroscopy is used to probe the band structure or molecular energy levels in the materials since UV-Vis light excitation creates photo-generated electron and holes (Reddy et al., 2001). Figure 35 and Figure 36 show the UV-Vis diffused reflectance spectra of Al-doped TiO_2 samples and B-doped TiO_2 samples, respectively. The UV-Vis

spectrum of these trivalent (Al, B)-doped TiO_2 samples are steep line in comparision to the undoped TiO_2 sample. Their absorption edge shows the mixed value of anatase and rutile structure which more similar to those of bulk rutile than anatase phase. This could be attributed to the higher content of rutile in sample. The onset of absorption and band gap energy of these trivalent (Al, B)-doped TiO_2 samples are shown in Tables 25 and 26. These could be seen that the onsets of Al-doped TiO_2 samples are lower than that the undoped TiO_2 sample, except some calcined_Al/TiO_2 samples have equal or more than the absorption edge of the undoped TiO_2 sample. In the case of B-doped TiO_2 samples, these onset of absorption are lower than that the undoped TiO_2 sample, but calcined_B/TiO_2 samples show higher onset of absorption than that the undoped TiO_2 sample. The position of the absorption edge for most of these trivalent (Al, B)-doped TiO_2 samples are blue-shifted in comparision with the undoped TiO_2 sample, the quantum-size effect is notable for these catalysts. Furthermore, it could be obvious in calcined_B/TiO_2 samples show red-shifted in comparision with the undoped TiO_2 sample. The onset of as-prepared samples were in the range 378-420 nm corresponding to the electron transition from the valence band which composed of 2p atomic orbitals of oxygen (π band orbitals) to the conduction band which originated from the 3d atomic orbitals of titanium (Sanchez et al., 1995), giving the band gap energy of the undoped TiO_2 sample and these trivalent (Al, B)-doped TiO_2 samples, these band gap energy value are shown in Tables 25 and 26. It should be noticed that there was the difference in band gap energy between these synthesized TiO_2 samples. This phenomenal might be result of the smaller particle size, poor crystallinity and also defects on crystal planes of undoped TiO_2 sample (Zhang et al., 2000). It had been known that the properties of nanosized semiconductor particles have been long known to depend very sensitively on the particle size. This is the so-called "quantum size effect". As the diameter of crystallite approaches the exciton Bohr diameter, a splitting of the energy bands into discrete quantized energy level occur, it leads to a blue-shift in the absorption spectrum due to increased band gap nonlinear optical properties (Reddy et al., 2001). Thus, it means that as the particle size decrease the band gap energies increase. In order to determine the nature of the band gap and the type of band-to-band transition in synthesized titanium dioxide, either indirect or direct transition one has to consider the expression for the variation of the absorption coefficient with energy.

Firstly, to establish the type of band-to-band transition in the synthesized titanium dioxide particles, the absorption data were fitted to equations for both indirect or direct bandgap

transition. Figures 37-40 show the plot of $(\alpha E_{phot})^{1/2}$ versus E_{phot} for an indirect transition and $(\alpha E_{phot})^{2}$ versus E_{phot} for a direct transition, respectively. The value of E_{phot} extrapolated to $\alpha = 0$ gives an absorption energy which corresponds to a band gap energy (E_{g}). As seen in Figures 37 and 38 for indirect transition and Figures 39 and 40 for direct transition of the undoped TiO_2 sample and these trivalent (Al, B)-doped TiO_2 samples. The results show a perfect fit and the extrapolation yields an E_{g} value which shown in Tables 22 and 23. For this study shows that the band-to-band transition in synthesized titanium dioxide samples were fitted to the direct bandgap transition. This result is in agreement with the work of Sepone et al., (1995) who had established the mechanism believed being operatively in nanophase titanium dioxide. They had attributed the spectral blue shifts due to quantum size effects in titanium dioxide colloids as a result of direct transitions (Serpane et al.,1995).

4.2.9 Wavelength dispersive X-ray fluorescence spectrometry (WDXRF)

The XRF study gives a qualitative information about the detection of each element on the surface of as-prepared TiO_2 samples. From XRF spectrum of Al-doped TiO_2 sample and B-doped TiO_2 sample are shown in Figures 41 and 42. The results show trace amount of S, Si, and residual Cl (besides the two main elements : Ti and Al) for the data of Al-doped TiO_2 sample and contained trace amount of Ca, S, and Si element (besides the main elements : Ti) for the data of B-doped TiO_2 sample. In the case of Al-doped TiO_2 sample, concentrated in amount of Al dopants indicating that increasing amount of Al dopants also give more percentage of Al element on the Al-doped TiO_2 sample. For B-doped TiO_2 spectrum B element could not be found due to the limitation of the instrument.

4.3 Photocatalytic activities of methylene blue by undoped TiO_2 sample, commercial P25-TiO_2 sample and trivalent (Al, B)-doped TiO_2 samples.

The degradation of methylene blue (MB) was investigated by using the as-prepared trivalent (Al, B)-doped TiO_2 samples, undoped TiO_2 sample, and commercial P25-TiO_2 sample under UV irradiation. The UV source used in this work was the 20 watt backlight tube, which emits UV light in the range 346-395 nm with a maximum at 366 nm. The UV-Vis spectra of MB aqueous solution catalyzed by Al-doped TiO_2 samples and B-doped TiO_2 samples under different irradiation times are displayed in Figure 49 and Figure 50, respectively. The aqueous solution of methylene blue (MB, 2.5×10^{-5} M) shows a major absorption band at 656 nm and minor absorption band at 614 nm in the absence of synthesized TiO_2 samples.

In mixing TiO_2 catalysts with MB solution for the photocatalysis experiments, the adsorption of MB on the catalyst surface took place instantly prior to the photocatalytic measurements. In this experiments, the adsorption took place in 1 hour to reach their corresponding saturation point in the dark prior to irradiation with UV light, reflecting the extent of adsorption of MB molecule on the surface of these as-prepared TiO_2 catalysts. The relative MB remained (C/C_o) of these trivalent (Al, B)-doped TiO_2 samples as a function of time of adsorption are shown in Tables 28 and 29. The data of amount of MB adsorbed on TiO_2 catalysts surface are shown in Tables 30 and 31. Tables 28-31 indicated that the data of MB molecule adsorbed on the surface of these trivalent (Al, B)-doped TiO_2 catalysts agreed with the data of the remained of MB solution C/C_o. The results from the photocatalytic experiment at different irradiation time (1.5, 3.0, 4.5, and 6.0 h) are shown graphically in the term of remained of MB solution C/C_o monitoring at wavelenght 614 nm and   656 nm (Figures 51-52 for the trivalent (Al, B)-doped TiO_2 catalysts). From these photocatalytic activity, show that most of these as-prepared TiO_2 catalysts could be degrade the dye molecule into colorless of final MB solution under UV irradiation time. The color of MB solution after irradiation for 6 h of most of these synthesized samples are colorless. Therefore, we choose to measure the percentage of degradation MB at the irradiation time at 3 h, these results are shown in Tables 32 and 33. The resulting data from Tables 27 and 28 indicated that all synthesized trivalent (Al, B)-doped TiO_2 samples have lower photocatalytic efficiency than that commercial Degussa P25-TiO_2 catalysts.

Table 28 The relative remained of MB solution (C/C$_o$) as a time of adsorption (1 h) for Al-doped TiO$_2$ samples.

Al doped TiO$_2$ samples	The relative remained of MB (C/C$_o$) (average)*	
	At 614 nm	At 656 nm
undoped TiO$_2$	0.5778	0.6668
P25- TiO$_2$	0.4430	0.5090
a)amount_Al/TiO$_2$		
1_Al/TiO$_2$	0.7113	0.7804
2_Al/TiO$_2$	0.7390	0.8002
3_Al/TiO$_2$	0.8438	0.8886
4_Al/TiO$_2$	0.8279	0.8437
b)water_Al/TiO$_2$		
50w_Al/TiO$_2$	0.4634	0.5234
100w_Al/TiO$_2$	0.7113	0.7804
150w_Al/TiO$_2$	0.7021	0.7329
200w_Al/TiO$_2$	0.7119	0.8075
c)acid_Al/TiO$_2$		
CH$_3$COOH_Al/TiO$_2$	0.7098	0.7769
HCl_Al/TiO$_2$	0.7113	0.7804
HNO$_3$_Al/TiO$_2$	0.6224	0.6846
H$_2$SO$_4$_Al/TiO$_2$	0.8010	0.8130
H$_3$PO$_4$_Al/TiO$_2$	0.0174	0.0191
d)calcined_Al/TiO$_2$		
400c_Al/TiO$_2$	0.8203	0.8338
500c_Al/TiO$_2$	0.8198	0.8859
600c_Al/TiO$_2$	0.8942	0.9414
700c_Al/TiO$_2$	0.8986	0.9606
800c_Al/TiO$_2$	0.9420	0.9436

* n = 3

Table 29 The relative remained of MB solution (C/C_o) as a time of adsorption (1 h) for B-doped

TiO$_2$ samples.

B doped TiO$_2$ samples	The relative remained of MB (C/C_o) (average)*	
	At 614 nm	At 656 nm
undoped TiO$_2$	0.5778	0.6668
P25- TiO$_2$	0.4430	0.5090
a)amount_B/TiO$_2$		
0.5wt_B/TiO$_2$	0.4924	0.5634
1.0wt_B/TiO$_2$	0.5659	0.6665
2.0wt_B/TiO$_2$	0.7875	0.8234
3.0wt_B/TiO$_2$	0.7077	0.8135
4.0wt_B/TiO$_2$	0.7921	0.8221
5.0wt_B/TiO$_2$	0.6304	0.7162
10.0wt_B/TiO$_2$	0.6424	0.7050
b)water_B/TiO$_2$		
50w_B/TiO$_2$	0.5989	0.7017
100w_B/TiO$_2$	0.4927	0.5634
150w_B/TiO$_2$	0.3529	0.3649
200w_B/TiO$_2$	0.1746	0.1857
c)acid_B/TiO$_2$		
CH$_3$COOH_B/TiO$_2$	0.5606	0.6438
HCl_B/TiO$_2$	0.4924	0.5334
HNO$_3$_B/TiO$_2$	0.3859	0.3794
H$_2$SO$_4$_B/TiO$_2$	0.8637	0.9239
H$_3$PO$_4$_B/TiO$_2$	0.0195	0.0221
d)calcined_B/TiO$_2$		
400c_B/TiO$_2$	0.6551	0.7402
500c_B/TiO$_2$	0.7475	0.8381
600c_B/TiO$_2$	0.8175	0.8655
700c_B/TiO$_2$	0.7705	0.8576
800c_B/TiO$_2$	0.6817	0.7628

* n = 3

224

Table 30 The amount of MB molecule adsorbed on the surface of Al-doped TiO_2 samples
(At 656 nm).

Al doped TiO_2 samples	MB adsorbed on catalysts surface (average)* (mg/g)
undoped TiO_2	1.2328
P25- TiO_2	1.8521
a)amount_Al/TiO_2	
1_Al/TiO_2	1.1033
2_Al/TiO_2	0.9016
3_Al/TiO_2	0.2193
4_Al/TiO_2	0.3974
b)water_Al/TiO_2	
50w_Al/TiO_2	1.9929
100w_Al/TiO_2	1.1033
150w_Al/TiO_2	0.9668
200w_Al/TiO_2	1.0736
c)acid_Al/TiO_2	
CH_3COOH_Al/TiO_2	0.6821
HCl_Al/TiO_2	1.1033
HNO_3_Al/TiO_2	0.9965
H_2SO_4_Al/TiO_2	0.5693
H_3PO_4_Al/TiO_2	4.3895
d)calcined_Al/TiO_2	
400c_Al/TiO_2	0.6449
500c_Al/TiO_2	0.3737
600c_Al/TiO_2	0.3678
700c_Al/TiO_2	0.3322
800c_Al/TiO_2	0.3391

* n = 3

Table 31 The amount of MB molecule adsorbed on the surface of B-doped TiO_2 samples

(At 656 nm).

B doped TiO_2 samples	MB adsorbed on catalysts surface (average)* (mg/g)
undoped TiO_2	1.2328
P25- TiO_2	1.8521
a)amount_B/TiO_2	
0.5wt_B/TiO_2	2.3785
1.0wt_B/TiO_2	1.7447
2.0wt_B/TiO_2	1.1033
3.0wt_B/TiO_2	1.0380
4.0wt_B/TiO_2	1.0024
5.0wt_B/TiO_2	1.1626
10.0wt_B/TiO_2	1.5066
b)water_B/TiO_2	
50w_B/TiO_2	1.6549
100w_B/TiO_2	2.3785
150w_B/TiO_2	2.8263
200w_B/TiO_2	3.6556
c)acid_B/TiO_2	
CH_3COOH_B/TiO_2	1.6786
HCl_B/TiO_2	2.3785
HNO_3_B/TiO_2	2.7848
H_2SO_4_B/TiO_2	0.4982
H_3PO_4_B/TiO_2	4.3766
d)calcined_B/TiO_2	
400c_B/TiO_2	1.1329
500c_B/TiO_2	0.8067
600c_B/TiO_2	0.6881
700c_B/TiO_2	0.5338
800c_B/TiO_2	1.1329

* n = 3

Table 32 The percentage degradation of MB under irradiation time (3 h) for Al-doped TiO_2

samples (including adsorption).

Al doped TiO_2 samples	% Degradation of MB (average)*	
	At 614 nm	At 656 nm
undoped TiO_2	94.16	98.37
P25- TiO_2	99.58	99.56
a)amount_Al/TiO_2		
1_Al/TiO_2	77.19	97.79
2_Al/TiO_2	70.37	80.69
3_Al/TiO_2	29.92	18.80
4_Al/TiO_2	31.39	26.15
b)water_Al/TiO_2		
50w_Al/TiO_2	96.21	98.72
100w_Al/TiO_2	77.19	97.79
150w_Al/TiO_2	85.35	93.64
200w_Al/TiO_2	95.40	96.14
c)acid_Al/TiO_2		
CH_3COOH_Al/TiO_2	43.41	46.32
HCl_Al/TiO_2	77.19	97.79
HNO_3_Al/TiO_2	78.25	97.35
H_2SO_4_Al/TiO_2	38.80	27.55
H_3PO_4_Al/TiO_2	98.14	98.77
d)calcined_Al/TiO_2		
400c_Al/TiO_2	30.57	29.34
500c_Al/TiO_2	23.17	16.47
600c_Al/TiO_2	19.70	13.99
700c_Al/TiO_2	25.79	17.79
800c_Al/TiO_2	33.94	26.21

* n = 3

Table 33 The percentage degradation of MB under irradiation time (3 h) for B-doped TiO_2 samples (including adsorption).

B doped TiO_2 samples	% Degradation of MB (average)*	
	At 614 nm	At 656 nm
undoped TiO_2	94.16	98.37
P25- TiO_2	95.58	99.56
a)amount_B/TiO_2		
0.5wt_B/TiO_2	91.89	97.79
1.0wt_B/TiO_2	89.34	98.08
2.0wt_B/TiO_2	85.07	98.67
3.0wt_B/TiO_2	84.91	98.84
4.0wt_B/TiO_2	84.09	98.93
5.0wt_B/TiO_2	84.28	97.98
10.0wt_B/TiO_2	80.36	97.22
b)water_B/TiO_2		
50w_B/TiO_2	93.23	98.15
100w_B/TiO_2	91.89	97.79
150w_B/TiO_2	97.01	98.75
200w_B/TiO_2	96.48	98.86
c)acid_B/TiO_2		
CH_3COOH_B/TiO_2	93.11	98.37
HCl_B/TiO_2	91.89	97.79
HNO_3_B/TiO_2	94.41	98.35
H_2SO_4_B/TiO_2	40.63	37.16
H_3PO_4_B/TiO_2	97.42	98.39
d)calcined_B/TiO_2		
400c_B/TiO_2	50.44	93.36
500c_B/TiO_2	41.21	73.13
600c_B/TiO_2	49.28	70.78
700c_B/TiO_2	63.32	72.74
800c_B/TiO_2	81.90	91.56

* n = 3

In the case of the simple photocatalytic reaction under UV-light irradiation, the degradation of MB should go through the interaction with the electron-hole pair (e_{CB}^{-} - h_{VB}^{+}) as usual. The proposed MB degradation mechanism for the irradiated TiO_2 system is summarized in Figure 60.

1. $TiO_2 + h\nu \rightarrow e_{CB}^{-} + h_{VB}^{+}$

2. $(O_2)_{ads} + e_{CB}^{-} \rightarrow O_2^{\bullet -}$

3. $(H_2O \leftrightarrow H^{+} + OH^{-})_{ads} + h_{VB}^{+} \rightarrow H^{+} + OH^{\bullet}$

4. $O_2^{\bullet -} + H^{+} \rightarrow HO_2^{\bullet}$

5. $2\, HO_2^{\bullet} \rightarrow H_2O_2 + O_2$

6. $H_2O_2 + e^{-} \rightarrow OH^{\bullet} + OH^{-}$

7. $R_{(ads)} + OH^{\bullet} \rightarrow$ degradation products

8. $R_{(ads)} + h_{VB}^{+} \rightarrow$ degradation products
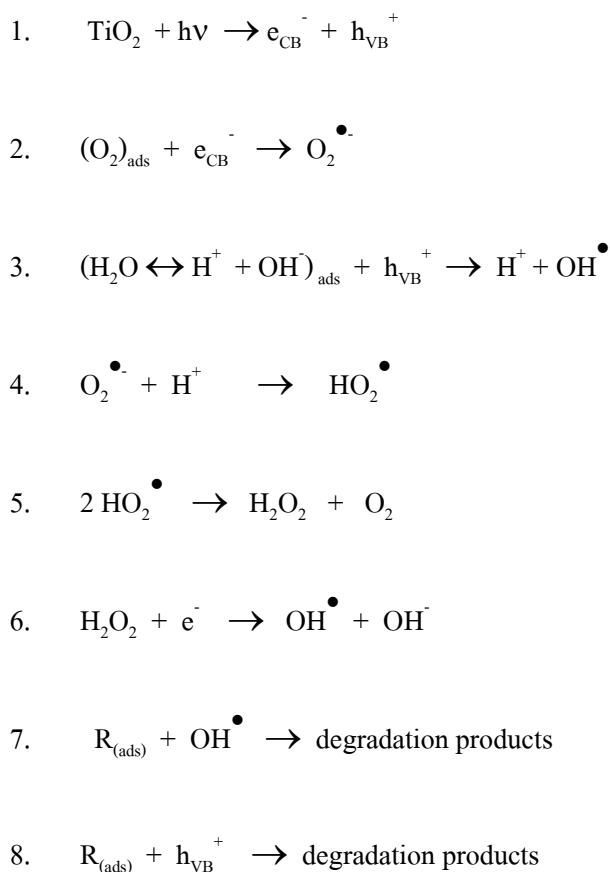
Figure 60 Possible steps involved in MB degradation by TiO_2 photocatalyst (Houas, etal., 2001).

In step (2) of Figure 60, $(O_2)_{ads}$ comes from the O_2 that was present in the system and was adsorbed onto the surface of the catalyst. In the degrading of MB, step (7) R = MB and since MB has a cationic configuration it should be favourably adsorbed to the negative sites of the as-prepared TiO_2 surface, e.g., Ti-O $^{(-)}$ and subsequently attacked by the very active $OH^{\bullet}$, leading to the destruction of the MB molecule. This results agree with their work of Randorn et al. (2004) who investigated bleaching of methylene blue by hydrated titanium dioxide (h-TiO_2) catalyst. They found that h-TiO_2 can adsorbed a large amount of methylene blue on its surface, abount nine times as much of

Degussa P25-TiO$_2$. In the present of dilute H$_2$O$_2$ and with UV light, h-TiO$_2$ can bleach methylene blue as well as Degussa P25-TiO$_2$. However, under similar conditions, but without UV light, h-TiO$_2$ can bleach methylene blue much better than Degussa P25-TiO$_2$ (Randorn et al., 2004).

Kiriakidou et al., (1999) investigated the effect of incorporating cations with valence higher (W^{6+}) and lower (Ca^{2+}) than the present cation (Ti^{4+}) in the TiO$_2$ matrix. They found that doping of TiO$_2$ with cations of valence higher than that of the present Ti^{4+} cation results in increased concentration of electrons in the conduction band as illustrated by the following defect site reaction;

$$WO_3 \leftrightarrow W[Ti]^{2+} + \frac{1}{2}O_2 + 2e^-$$
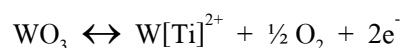
As the n-dopant concentration increases the surface barrier becomes higher and the space charge region narrower. The electron-hole pairs photogenerated within this region are efficiently separated by the large electric field traversing the barrier, before having the chance to recombine. When TiO$_2$ is doped with lower valence cations the opposite behavior is expected. In this case, doping results in increased concentration of holes in the valence band, as illustrated by the following defect site reaction;

$$CaO + \frac{1}{2}O_2(g) + 2e^- \leftrightarrow Ca[Ti]^{2-} + TiO_2$$
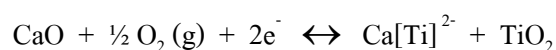
As the p-dopant concentration increased, the surface barrier is lowered and the space charge region becomes progressively thicker (Kiriakidou et al., 1999).

In present work, the trivalent (Al, B) are lower valence cations than the present Ti^{4+} cation in the TiO$_2$ matrix. The photocatalytic degradation behavior of dye molecule could be explained following the same rationale as in the case of Ca^{2+} doped TiO$_2$ of Kiriakidou's work.